Arabian Journal of Chemistry (2021) **14**, 102909

King Saud University

Arabian Journal of Chemistry

www.ksu.edu.sa
www.sciencedirect.com

ORIGINAL ARTICLE

Part II: Impact of ionic liquids as anticorrosives and additives on Ni-Co alloy electrodeposition: Experimental and DFT study

Inam M.A. Omar [a,b], **Abdo Mohammed Al-Fakih** [a,c,*], **Madzlan Aziz** [a], **Khadijah M. Emran** [b]

[a] *Department of Chemistry, Faculty of Science, Universiti Teknologi Malaysia, Johor Bahru, Johor, Malaysia*
[b] *Chemistry Department, College of Science, Taibah University, Al-Madinah Al-Monawarah, Saudi Arabia*
[c] *Department of Chemistry, Faculty of Science, Sana'a University, Sana'a, Yemen*

Received 23 August 2020; accepted 3 November 2020
Available online 16 November 2020

KEYWORDS

Ni-Co alloy;
Electrodeposition;
Ionic liquid;
Corrosion;
EIS;
DFT

Abstract The impacts of 1-methyl-3-(2-oxo-2 ((2,4,5trifluorophenyl)amino)ethyle)-1H-imidazol-3-ium iodide ([MOFIM]I) and 1-(4-fluorobenzyl)-3-(4-phenoxybutyl)imidazol-3-ium bromide ([FPIM]Br) ionic liquids as additives on the corrosion behavior and the electrodeposition nucleation mechanism of a Ni-Co alloy were elucidated. A systematic investigation of the corrosion protection ability of Ni-Co alloys in a 3.5% NaCl solution was carried out using Tafel polarization and electrochemical impedance spectroscopy (EIS) studies. The mechanism of the Ni-Co alloy electrodeposition from the Ni70-Co30 bath was investigated using potentiodynamic cathodic polarization, cyclic voltammetry (CV) and anodic linear stripping voltammetry (ALSV). The studied ionic liquids (ILs) inhibit Co^{2+} and Ni^{2+} ion deposition due to their adsorption, which obeys the Langmuir adsorption isotherm. Quantum chemical calculations were performed at the B3LYP/6-311++G(d,p) level of the density functional theory (DFT). Several quantum parameters and natural atomic charges were calculated to investigate the correlation between the molecular structures of [MOFIM]I and [FPIM]Br and their corrosion inhibition performance. [MOFIM]I at 1×10^{-5} M

---

[*] Corresponding author at: Department of Chemistry, Faculty of Science, Universiti Teknologi Malaysia, Johor Bahru, Johor, Malaysia; Department of Chemistry, Faculty of Science, Sana'a University, Sana'a, Yemen.

E-mail addresses: emomar@taibahu.edu.sa (I.M.A. Omar), aalfakih2011@gmail.com (A.M. Al-Fakih), madzlan@utm.my (M. Aziz), kabdalsamad@taibahu.edu.sa (K.M. Emran).

Peer review under responsibility of King Saud University.

ELSEVIER **Production and hosting by Elsevier**

https://doi.org/10.1016/j.arabjc.2020.11.015

1878-5352 © 2020 The Author(s). Published by Elsevier B.V. on behalf of King Saud University.
This is an open access article under the CC BY-NC-ND license (http://creativecommons.org/licenses/by-nc-nd/4.0/).

shows a higher inhibition efficiency (IE%) of 53.05% than [FPIM]Br, at 44.3%. The results show that the calculated values of the quantum parameters are consistent with the experimental findings.

© 2020 The Author(s). Published by Elsevier B.V. on behalf of King Saud University. This is an open access article under the CC BY-NC-ND license (http://creativecommons.org/licenses/by-nc-nd/4.0/).

1. Introduction

Metal corrosion is a serious issue because corrosion causes a waste of resources, reducing the lifetime of equipment and negatively affecting the environment (Al-Fakih et al., 2019). Therefore, the protection of industrial materials from corrosion processes is of paramount importance, not only to maximize the durability of appliances but also to diminish the transfer of toxic metals from industrial materials to the environment (Kumar et al., 2019). The demand for increasing the longevity of metals or alloys is drastically increasing due to their wide applications in engineering practice (Al Radadi and Ibrahim, 2020; Omar et al., 2020). Ni-Co alloy coatings achieved by the electrodeposition method have been widely studied due to their promising features, such as their superior corrosion resistance, low expense, ease of maintenance, uniform coating thickness and use in the production of high quality alloys. The electrodeposition technique can handle complex geometries and shows low toxicity, unlike other coating technologies, e.g., physical and chemical vapor deposition (Al Radadi and Ibrahim, 2020). Nanocrystalline Ni-Co alloy as a surface coating is receiving considerable attention because its potential applications are multitudinous (Ibrahim et al., 2016).

Ionic liquids (ILs) are salts composed of highly asymmetric ions consisting of an organic cation with an organic or inorganic anion that remain in the liquid state at temperatures less than 100 °C and even, in many cases, at room temperature (Carlesi et al., 2016). The use of ILs as electrolytes for metal or alloy electrodeposition has increased in recent years (Anicai et al., 2019; Bakkar and Neubert, 2020; Sun et al., 2020; Alesary et al., 2019; Vijayakumar et al., 2013). Particular attention has been paid to ILs as promising alternatives due to their unique physicochemical properties (Ibrahim et al., 2016; Anicai et al., 2019). However, a few published works have discussed using ILs as additives in Ni-Co alloy electrodeposition processes (Carlesi et al., 2016; Qibo and Yixin, 2017). The importance of additives in the electrodeposition process comes from their roles in efficiently improving the surface morphology and in crystal-building of the deposit by inhibiting crystal growth towards other crystallographic axes (Hashemi et al., 2017). In the current work, the effect of two novel synthesized ILs namely 1-methyl-3-(2-oxo-2-((2,4,5 trifluorophenyl) amino) ethyl)-1H-imidazol-3-ium iodide ([MOFIM]I) and 1-(4-fluorobenzyl)-3-(4-phenoxybutyl)imidazol-3-ium bromide ([FPIM]Br) on the Ni-Co alloy coatings from a sulfate bath was studied for the first time as new ionic liquid addition agents in Ni-Co alloy electrodeposition.

Traditionally, experimental techniques are mainly used to study the performance of additives in the electrodeposition field. However, experimental procedures are expensive, time consuming and harmful to the environment (Al-Fakih et al., 2019). Therefore, it is economical, fast, and ecofriendly to apply computational techniques, such as quantum chemical calculations, as predictive techniques. Density functional theory (DFT) is a quantum chemical approach that is considered a powerful tool to calculate several quantum parameters of molecules with reasonable accuracy. Several quantum parameters, such as highest occupied molecular orbital energy (E_{HOMO}), lowest unoccupied molecular orbital energy (E_{LUMO}), energy gap (ΔE), ionization potential (I), electron affinity (A), electronegativity (χ), hardness (η), softness (S) and fraction of electrons transferred from the inhibitor to the metal surface (ΔN), can be calculated using DFT (Al-Fakih, 2017). The quantum parameters are calculated to be used for theoretical investigations of corrosion inhibition properties and to predict the inhibition efficacies of additives as corrosion inhibitors based on their electronic/molecular properties and reactivity indices (Al-Fakih, 2017). Most studies use quantum chemical parameters of organic compounds as corrosion inhibitors (Al-Fakih et al., 2019; Al-Fakih, 2017; Murulana et al., 2016; Lukovits et al., 2001; El-Raouf et al., 2018; Sulaiman et al., 2019). However, the understanding of the behavior of ILs when used as additives in electrodeposition processes is limited and insufficient (Deng et al., 2018; Ren et al., 2015). Moreover, the natural atomic charge, i.e., Mulliken population analysis, has been calculated to determine the active sites and the adsorption mode of additives or inhibitor molecules, which can offer or accept electrons (El-Raouf et al., 2018). There is a general consensus that the more negatively charged the heteroatom is, the more adsorption centers there are on the metal surface through donor–acceptor interactions (El-Raouf et al., 2018). The use of Mulliken population analysis has been widely reported for calculation of the charge distribution over the whole skeleton of inhibitor molecules (Al-Fakih et al., 2019; Kumar et al., 2019).

In our recent study (Omar et al., 2020); The Ni-Co alloy co-electrodeposit from a sulfate bath including two new ionic liquids [MOFIM]I and [FPIM]Br as additives under three different [Ni^{2+}] and [Co^{2+}] concentrations was characterized using the SEM, EDS, EDS mapping, XRD, AFM and microhardness measurement techniques. The addition of 1×10^{-5} M [MOFIM]I and [FPIM]Br in a bath with a composition of Ni70%-Co30% led to optimal Ni-Co alloy coatings, which exhibited characteristics such as finer grains, and a more coherent and compact deposit, as verified by SEM and AFM measurements. However, [MOFIM]I served as more effective leveling agents by obtaining finer grains and more oriented crystals than [FPIM]Br. The optimal bath conditions that led to the highest CCE% values for the co-electrodeposition of the Ni-Co alloys involved a current of 20 mA cm^{-2}, deposit potential of 6.5 V, pH of 4.5, temperature of 20 °C and deposit time of 10 min. The CCE% values attained maximum values of 99.8% and 97.07% in the presence of [MOFIM]I and [FPIM]Br, respectively, under the composition of Ni 70% and Co 30%. In all the considered Ni-Co alloy coatings corresponding to baths 1–9, the Co content (the less noble metal) in the alloy was higher than that in the bath, thereby indicating that the codeposition of Co and Ni corresponded to anomalous plating.

Although the characterization and microhardness of Ni-Co alloy co-electrodeposit from bath including [MOFIM]I and [FPIM]Br was achieved using variety techniques, but Ni-Co alloy is lack to investigated the corrosion resistance which is considered as more important properties of coating in many industrials fields. Moreover, the favorable morphology of Ni-Co alloy deposits is resulted of an effective role of both considered ILs during co-electrodeposition process. In our lasts work (Part I) (Omar et al., 2020); it was expected that both the considered ILs led to favorable results as they inhibited the Ni^{2+} and Co^{2+} reduction owing to the adsorption of the IL cations on the energetically favorable surfaces on the substrate and the first stages of the Ni-Co alloy deposits. Owing to this adsorption, the ILs hindered the H_2 evolution, controlled the grain growth and increased the nucleation rate.

Therefore, the present study aims to investigate the inhibition efficiencies of two novel imidazole derivatives, [MOFIM]I and [FPIM]Br, and the corrosion resistance of Ni-Co alloy coatings on Cu substrates from a sulfate bath using potentiodynamic polarization and EIS. Moreover, potentiodynamic cathodic polarization, cyclic voltammetry (CV) and anodic linear stripping voltammetry (ALSV) were used to determine the nucleation mechanism of Ni-Co alloy electrodeposition. The study also evaluated the experimental inhibition efficiencies of two ILs via quantum chemical calculations as a computational approach. DFT was used to optimize the molecular structures of [MOFIM]I and [FPIM]Br. The quantum chemical parameters and natural atomic charge of [MOFIM]I and [FPIM]Br were also calculated to investigate their active sites and the electronic interactions between the studied ILs and Ni-Co alloy coating surface.

2. Experimental and theoretical details

2.1. Coating fabrication

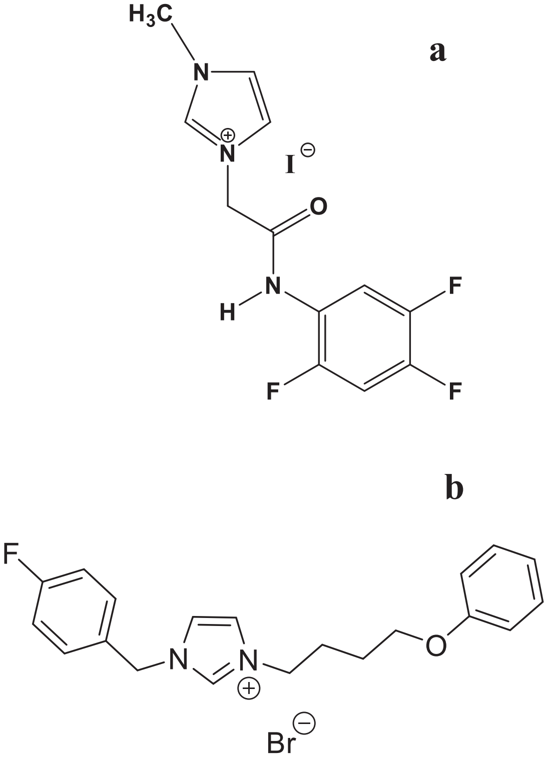

Fig. 1 Ionic liquids (a) (1-methyl-3-(2-oxo-2-((2,4,5 trifluorophenyl)amino)ethyle)-1H-imidazol-3-ium iodide) [MOFIM]I, (b) 1-(4-fluorobenzyl)-3-(4-phenoxybutyl)imidazol-3-ium bromide [FPIM]Br.

Electrodeposition of the Ni-Co alloy onto a Cu substrate (99.9% in purity) was performed using an acidic sulfate bath with three different compositions of [Ni^{2+}] and [Co^{2+}] in the absence and presence of [MOFIM]I and [FPIM]Br (Table 1). All chemicals and reagents were of analytical grade, and the electrolytes were freshly prepared using doubly distilled water. pH was adjusted using 1:1 (H_2SO_4:H_2O) and was measured using a pH meter (HANNA, IH 2210, ITALY). Before each experiment, the Cu sheets were cleaned in a pickling solution (300 ml H_2SO_4, 100 ml HNO_3, 5 ml HCl and 595 ml H_2O) (Al Raddadi, 2014) for 20 s and then rinsed with distilled water and dried in a desiccator. A rectangular trough was used as a deposition cell, supplementary material (T1).

The imidazolium iodide incorporating aromatic amide, namely, 1-methyl-3-(2-oxo-2-((2,4,5-trifluorophenyl) amino) ethyle)-1H-imidazol-3-ium iodide (MOFIM]I), M.W = 397.15 g/mol, was synthesized through simple quaternization of methylimidazole with fluorinated aromatic acetamide bromide in acetonitrile (Rezki et al., 2020), as shown in Fig. 1a. The imidazolium bromide, namely, 1-(4-fluorobenzyl)-3-(4-phenoxybutyl)imidazol-3-ium bromide ([FPIM]Br), M.W = 405.31 g/mol, was ultrasonically synthesized as reported in (Omar et al.,

Table 1 The composition of Ni-Co alloys baths in absence and presence of [MOFIM]I and [FPIM]Br, at 30 g/L [H_3BO_3].

	Ni70%-Co30% bath			Ni50%-Co50% bath			Ni30%-Co70% bath		
Bath composition g/L (Deng et al., 2018)	Bath1	Bath2	Bath3	Bath4	Bath5	Bath6	Bath7	Bath8	Bath9
$NiSO_4{\cdot}6H_2O$	70	70	70	50	50	50	30	30	30
$CoSO_4{\cdot}7H_2O$	30	30	30	50	50	50	70	70	70
[MOFIM]I	0	1×10^{-5}	0	0	1×10^{-5}	0	0	1×10^{-5}	0
[FPIM]Br	0	0	1×10^{-5}	0	0	1×10^{-5}	0	0	1×10^{-5}

2020) and as shown in Fig. 1b. The newly synthesized MOFIM]I and[FPIM]Br were characterized using several spectroscopic methods, such as 1H and 13C, as reported in (Rezki et al., 2020; Omar et al., 2020).

Electrodeposition of the Ni-Co alloy was carried out cathodically by supplying direct current using a DC power supply unit (QJ3005A, ITALY) under three different bath compositions, Table 1, and the conditions, at different current densities, potentials, 10 mints, 25 °C and pH 4.5 without and with different concentrations of [MOFIM]I and [FPIM]Br, supplementary material (T1). A Cu substrate flat sheet and a platinum (Pt) sheet were used as the cathode and anode, respectively, with the same dimensions. Both cathode and anode were fixed at rectangular deposition cell.

2.2. Corrosion resistance measurements

The corrosion behavior of the Ni-Co alloy codeposits in a marine environment (a 3.5% NaCl solution) at 25 °C was evaluated using open circuit potential (OCP), potentiodynamic polarization and electrochemical impedance spectroscopic (EIS) tests. In this regard, a three-electrode corrosion cell was used for electrochemical measurements as well. A Pt sheet was used as the counter electrode (CE), SCE as the reference electrode (RE) and Ni-Co alloy coated samples as the working electrode (WE). All samples were first immersed in the 3.5% NaCl solution for approximately 30 min to stabilize the OCPs. EIS measurements were carried out over a frequency range between 100 kHz and 0.01 Hz with a 10 mV amplitude superimposed AC signal, and the corresponding Nyquist plot was obtained. Then, potentiodynamic curves with 1 mVs^{-1} were recorded by scanning from ± 700 mV from OCP. The inhibition efficiencies (IE_{Rct}) were calculated from the charge transfer resistance values using the following eq. (Al-Fakih, 2017):

$$IE_{Rct} = \frac{R_{ct(IL)} - R_{ct}}{R_{ct(IL)}} \times 100 \quad (1)$$

where $R_{ct(IL)}$ and R_{ct} are the charge transfer resistances with and without ILs, respectively.

2.3. Voltammetric measurements

All voltammetric measurements were carried out in a bath with a composition of Ni70%-Co30%, Table 1, at pH 4.5 (Ibrahim et al., 2016). Electrochemical experiments of the Ni-Co alloy were carried out in a three-electrode cell using a Gamry potentiostat/galvanostat (Gamry Interface 1000) connected to a PC and were analyzed using *Gamry Echem software*. Pt and SCE were used as the CE and RE, respectively. The Cu sheet or glassy carbon electrode (GCE) was used as the WE; the GCE was prepared as reported in (Omar et al., 2020). Potentiodynamic cathodic polarization curves were generated using the Cu sheet as the WE by sweeping the potential from the rest potential toward the less noble potentials, i.e., from −0.5 to −1.5 V_{SCE}, with a scan rate of 10 mV s^{-1} (Al Radadi and Ibrahim, 2020; Al Raddadi, 2014; Ibrahim and Al Radadi, 2020). The cyclic voltammetric (CV) measurements were performed in a three-electrode cell using a Gamry potentiostat/galvanostat (Gamry Interface 1000) connected to a PC and were analyzed using *Gamry Echem software*. Pt and SCE were used as the CE and RE, respectively. GCE was used as the WE in the potential range from 1.0 to −1.5 V_{SCE} with a scan rate of 100 mV s^{-1} (Al Radadi and Ibrahim, 2020; Al Raddadi, 2014; Ibrahim and Al Radadi, 2020). The working electrode was a GCE (a disk shaped area = 0.07 cm^2, 6 mm, reorder ET 051). GCE was polished with a polishing kit using an alumina slurry (α-alumina polishing powder 0.05 mm) until a mirror surface was obtained. Then GCE was rinsed with deionized water, and sonicated in ultrasonic bath for 5 min then dry the electrode under a stream of pure nitrogen. After electrodeposition, the produced coatings were rinsed by deionized water and ultrasonically treated to remove the deposits from the surface.

Situ-anodic linear stripping voltammetry (ALSV) measurements were performed at a constant potential (−1.0 V_{SCE}) on the GCE for 100 sec at 25 °C. At the end of each deposition time, stripping analysis was performed immediately in the same plating bath by sweeping the potential from −0.6 V_{SCE} to more anodic potentials (1.0 V_{SCE}) at a scan rate of 10 mV s^{-1} (Al Radadi and Ibrahim, 2020; Ibrahim and Al Radadi, 2020; El Sayed and Ibrahim, 2019) without removing the working electrode from the solution.

2.4. Theoretical calculations methodology

The molecular structures of the ionic liquid imidazole derivatives were sketched using Chem3D software. Gaussian09 software (Frisch et al., 2009) was used to perform geometry optimization and to calculate the quantum chemical parameters of the studied ionic liquids, including the neutral and cationic forms. The B3LYP level of the DFT method was used with the basis set 6-311++G(d,p). Several quantum chemical parameters were calculated, including E_{HOMO}, E_{LUMO}, ΔE, I, A, χ, η, S, t, ΔN and the natural atomic charge. All the quantum chemical calculations were performed in the gas phase. The values of all the quantum chemical parameters were calculated using the following equations (Eqs. (2)–(8)) (Al-Fakih, 2017; El Adnani et al., 2020; Belghiti et al., 2020; Rahmani et al., 2018; Bouoidina et al., 2019):

$$\Delta E = E_{LUMO} - E_{HOMO} \quad (2)$$

$$I = -E_{HOMO} \quad (3)$$

$$A = -E_{LUMO} \quad (4)$$

$$\chi = -\frac{1}{2}(E_{HOMO} + E_{LUMO}) \quad (5)$$

$$\eta = -\frac{1}{2}(E_{HOMO} - E_{LUMO}) \quad (6)$$

$$S = \frac{1}{\eta} \quad (7)$$

$$\Delta N = \frac{x}{2\eta} \quad (8)$$

3. Results and discussion

3.1. Electrochemical Impedance Spectroscopy (EIS)

To obtain detailed information of the electrode/electrolyte interface and to characterize the coating corrosion properties,

Table 2 The results from EIS and polarization measurements for the nine Ni-Co alloys deposits in 3.5% NaCl.

Bath No.	Alloy No.	Rct $(\text{k}\Omega\ \text{cm}^2)10^3\times$	CPE $10^{-6}\times$	n	IE %	W
Bath1	Ni-Co1	7.94	169.0	0.8952	–	137.0×10^{-6}
Bath2	Ni-Co2	16.92	119.8	0.8411	53.5	72.47×10^{-6}
Bath3	Ni-Co3	14.27	123.0	0.9305	44.3	21.83
Bath4	Ni-Co4	3.016	194.9	0.8704	–	7.257×10^{-3}
Bath5	Ni-Co5	4.161	212.9	0.8428	27.5	2.316×10^{-3}
Bath6	Ni-Co6	6.876	166.3	0.8863	56.2	1.003×10^{-3}
Bath7	Ni-Co7	1.051	250.5	0.8969	–	5.315×10^{-3}
Bath8	Ni-Co8	1.129	229.5	0.8530	6.9	38.95×10^{-3}
Bath9	Ni-Co9	1.642	216.8	0.9050	36.0	839.2

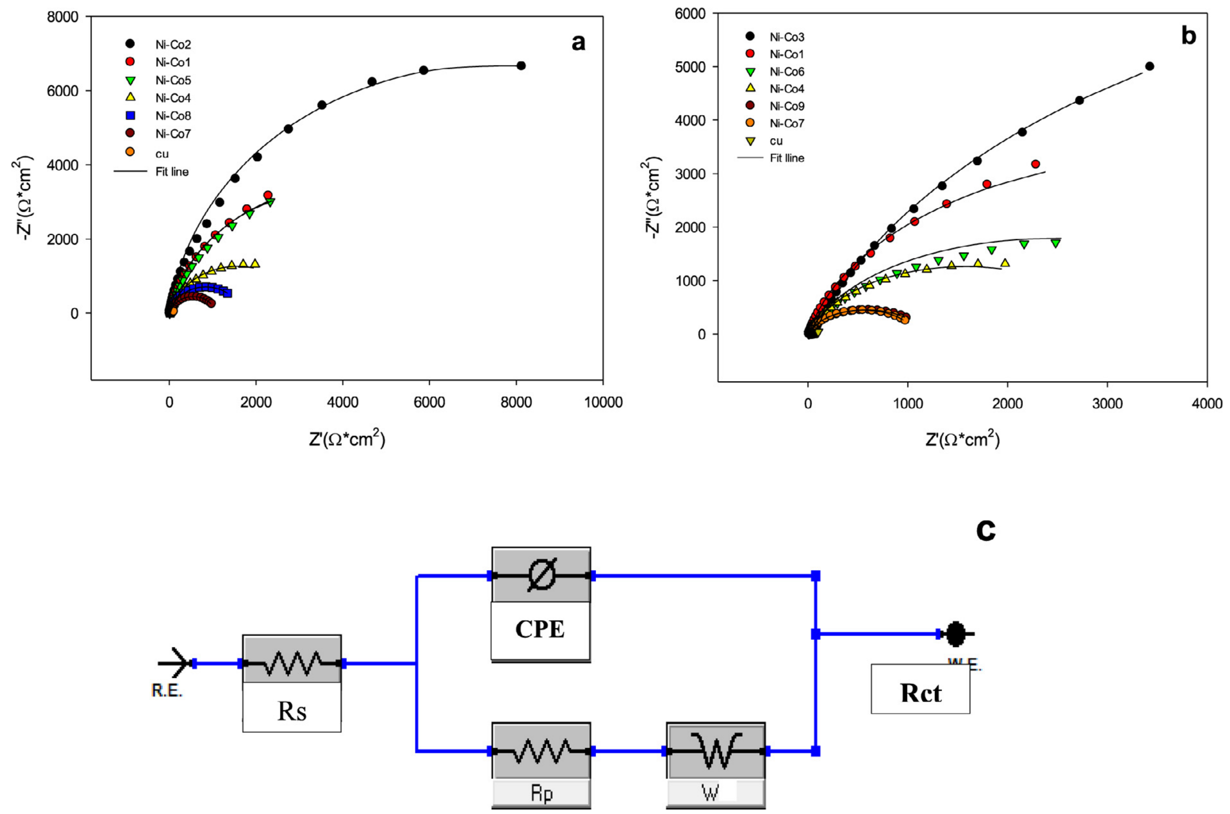

Fig. 2 Nyquist plots for Cu substrate, Ni-Co alloys in 3.5% NaCl without and with 1×10^{-5} M (a) [MOFIM]I, (b)[FPIM]Br (c) Equivalent circuit compatible with the experimental impedance data of Ni-Co alloy deposits.

EIS measurements of the Ni-Co alloy electrodeposited from nine different baths were carried out in the absence and presence of 1×10^{-5} M of both [MOFIM]I and [FPIM]Br in 3.5% NaCl. The charge transfer resistance (Rct), constant phase element (CPE), degree of roughness (n) and the Warburg impedance (W) parameters are listed in Table 2, with a $\chi 2$ of approximately 1×10^{-3}–1×10^{-6}. Fig. 2c shows the compatible equivalent circuits used to extract the parameters for the impedance spectra. The EIS in Fig. 2a, b revealed arc diameters with the following order: Ni-Co2 > Ni-Co3 > Ni-Co1 > Ni-Co6 > Ni-Co5 > Ni-Co4 > Ni-Co9 > Ni-Co8 > Ni-Co7. The capacitive loops for Ni-Co alloys deposited from free-ILs baths were always lower than those obtained from baths including [MOFIM]I and [FPIM]Br. It is well acknowledged that the width of the semicircle corresponds to the charge transfer resistance (R_{ct}) (Wang et al., 2019). The increase of the charge transfer impedance in the presence of ILs occurred without changing the corrosion behavior due to the formation of a protective layer on the deposit surface of the metal (Al-Fakih et al., 2019).

The R_{ct} values of the Ni-Co alloys gradually decrease with increasing Co^{2+} concentration in the bath. A similar behavior was reported in (Jiang et al., 2019). This result indicates that the Ni-Co1, Ni-Co2 and Ni-Co3 alloys (with $[Ni^{2+}]$ = 70 g/

L and [Co^{2+}] = 30 g/L) exhibited higher R_{ct} values than the other six alloys. R_{ct} is also associated with a decrease in CPE. The CPE values in Table 2 indicate a decrease in the local dielectric constant and/or an increase in the thickness of the electrical double layer due to the adsorption of the additive molecules onto the metal surface (Al-Fakih et al., 2019). Diffusion behavior is clearly observed in all nine Ni-Co alloys and the Warburg impedance (W) parameters are listed in Table 2. The high values of the degree of inhomogeneity (n) for the all alloys at the film/solution interface indicate the capacitive behavior of the alloy surfaces. The Ni-Co2 alloy deposited in the presence of 1×10^{-5} M [MOFIM]I has the largest R_{ct} among the nine alloys in this study. A higher R_{ct} corresponds to lower HER kinetics, as reported in (Wang et al., 2019). Moreover, R_{ct} can disclose the rate of corrosion. A lower R_{ct} value indicates a faster corrosion rate (El Sayed and Ibrahim, 2019). As a result, Ni-Co2 and Ni-Co3 could be the two best alloys to resist corrosion among all nine Ni-Co alloys examined in the current study. However, [MOFIM]I exhibited a higher effect against corrosion in the Ni-Co2 alloy than [FPIM]Br in the Ni-Co3 alloy due to the protective layer that formed on the electrode surface. It is worth mentioning the corrosion resistance of all nine Ni-Co alloys in the current study is higher than that of the Ni-Co-Sn alloy, R_{ct} 1.40 Ω cm^2, and the Ni-Co alloy, R_{ct} 340 Ω cm^2, which were obtained with saccharin as the additive (Chai and Jiang, 2019; Lokhande and Bagi, 2014) in a marine environment.

3.2. Comparison among Ni, Co and Ni-Co alloy electrodeposition

For comparison, Fig. 3a illustrates potentiodynamic cathodic polarization curves for the electrodeposition of Ni, Co and the Ni-Co1(Ni-Co blank) alloy, Table 1, under the operating conditions presented in supplementary material (T1). It is seen that the polarization curve for Ni deposition occurs at considerably more negative potentials than that of Co, which indicates that Ni is the nobler metal. Moreover, the polarization curve for the Ni-Co1 alloy lies between those of the parent metals. Codeposition enables the less noble metal (Co) to deposit at more positive potentials and causes the more noble metal (Ni) to deposit at more negative potentials than in the individual deposition. The data presented in Table 3 indicate that the Tafel slope, b_c, and the transfer coefficient, α_c, of the electrodeposition of the Ni-Co1 alloy are higher than those of Ni but lower than those of Co, while the i_o of the alloy is increased. Fig. 3b. shows typical CVs of the individual deposition of Ni and Co and the codeposition of the Ni-Co1 alloy under similar conditions as described in Table 1 and supplementary material (T1). The reduction peak of the Ni-Co1 alloy lies between those of Ni and Co, as in the polarization curves. The changes in the slopes of the cathodic part of the curves are due to an increase in the deposition rate. The anodic oxidation peak of the electrodeposition of Co was found to be higher than that of Ni or the Ni-Co1 alloy, indicating that Co will preferentially deposit under such conditions. The lower anodic oxidation peak of Ni than Co or the Ni-Co1 alloy indicates a small Ni fraction in the Ni-Co1 alloy. For comparison, the ALSVs for pure Ni, pure Co and the Ni-Co1 alloy under identical conditions are shown in Fig. 3c. It is obvious that the

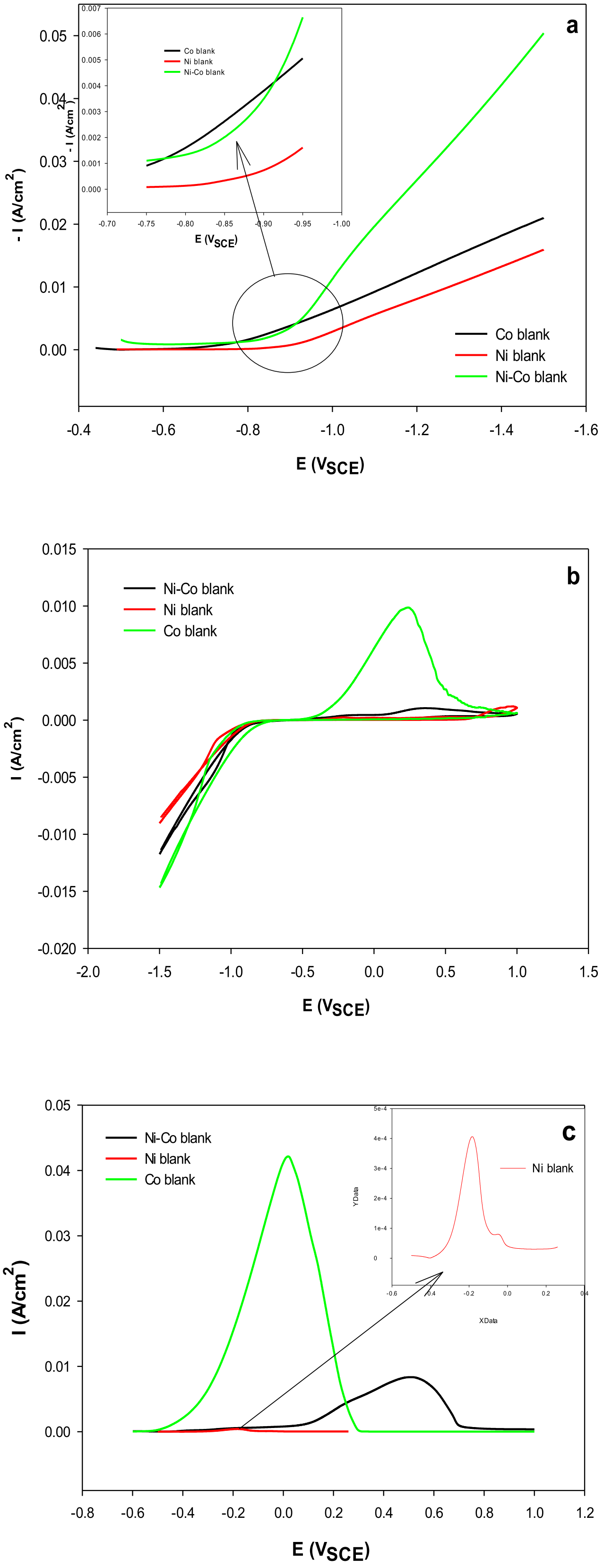

Fig. 3 Comparison among Ni, Co and Ni-Co alloy electrodeposition by voltametric measurments (a) potentiodynamic cathodic polarization curves, (b) CV, (c) ALSV.

Table 3 Tafel slope b_c and kinetic parameters of Ni, Co and Ni-Co1 alloy electrodeposition from acidic baths.

	b_c (mVdecade^{-1})	i_o (A cm^{-2})	α_c
Ni	−266	3.16×10^{-3}	0.0482
Co	−347	1.90×10^{-3}	0.0371
Ni-Co1 alloy	−278.4	6.16×10^{-3}	0.04611

stripping charge of pure Ni is very low compared to those of pure Co and the Ni-Co1 alloy. These results confirm the assumption that a cobalt-rich alloy is produced from bath1 at 25 °C.

3.3. Potentiodynamic cathodic polarization

Cathodic polarization curves were generated to investigate the effects of both the [MOFIM]I and [FPIM]Br ionic liquids on the Ni-Co alloys deposited from baths1, 2 and 3 (Table 3) with compositions of $[Ni^{2+}] = 70$ g/L and $[Co^{2+}] = 30$ g/L at pH 4.5 (Ibrahim et al., 2016); the curves are shown in Fig. 4a, b. In the free-ILs solutions, high polarization accompanies the deposition of the Ni-Co1 alloy, Ni-Co blank from bath1. The cathodic polarization potential (CPP) was approximately -0.93 V_{SCE} at 5.0×10^{-3} mA cm^{-2}, as shown in Table 4. A simultaneous discharge of hydrogen ions was observed during the deposition of the Co^{2+} and Ni^{2+} ions. The presence of 5×10^{-7} M [MOFIM]I caused a slight shift toward a more negative overpotential in the polarization curves compared to [FPIM]Br, as shown in Fig. 4a, b. A higher inhibition effect of [FPIM]Br was observed according to the CPP values in Table 4. This result is attributed to the formation of a more stable electrical double layer by the condensation product with electroactive functional groups (Shivakumara et al., 2008); as explained in the quantum calculation section of this work. The influences of [MOFIM]I and [FPIM]Br on hydrogen liberation may be explained by the hydrogen release mechanism; this mechanism is as follows (Lallemand et al., 2004):

$$H^+ + e \rightarrow H_{ads} \tag{9}$$

$$2H_{ads} \rightarrow H_2 \tag{10}$$

Both studied ILs are believed to block the association of electrolytically generated hydrogen atoms, Eq. (9), decreasing the concentration of H_{ads} and thus decreasing the rate of hydrogen evolution, Eq. (10). The inhibitory effect of the ILs could be attributed to their structures, which assist adsorption on the metal surface. As shown in Fig. 1a, b, both IL molecules contain a positive charge on the quaternary nitrogen atom of the imidazole ring. When electrical current is applied on the WE, the positively charged ILs (cations) are adsorbed to the energetically favored surfaces of the metal electrode (low energy surfaces), thus leaving only the high energy surfaces available for metal ion deposition (Hashemi et al., 2017). This process produces a network of this cationic ionic liquid on the electrode surface and hinders the formation of large Ni-Co alloy crystals.

3.4. Tafel lines and electrode kinetics

The kinetic parameters, such as the Tafel slope (b_c), η, overpotential and exchange current density (i_c), for Ni-Co alloy electrodeposition on copper were calculated by applying the Tafel equation, Eq. (11), as reported in (Sorour et al., 2017) from the cathodic polarization curves shown in Fig. 4

$$\eta_c = a + b_c \log i_c \tag{11}$$

The transfer coefficient (α_c) can be determined from Eq. (12.)

$$b = RT/\alpha nF \tag{12}$$

where n is the number of electrons and R and F are always the gas constant and Faraday's constant, respectively. The results presented in Table 5 reveal that b_c decreased as the [MOFIM]I concentration increased but fluctuated with [FPIM]Br during Ni-Co alloy reduction. The slight changes in b_c and α_c confirm that there was no change in the mechanism of the reduction process (Zhang and Hua, 2012). Table 5 shows that as the con-

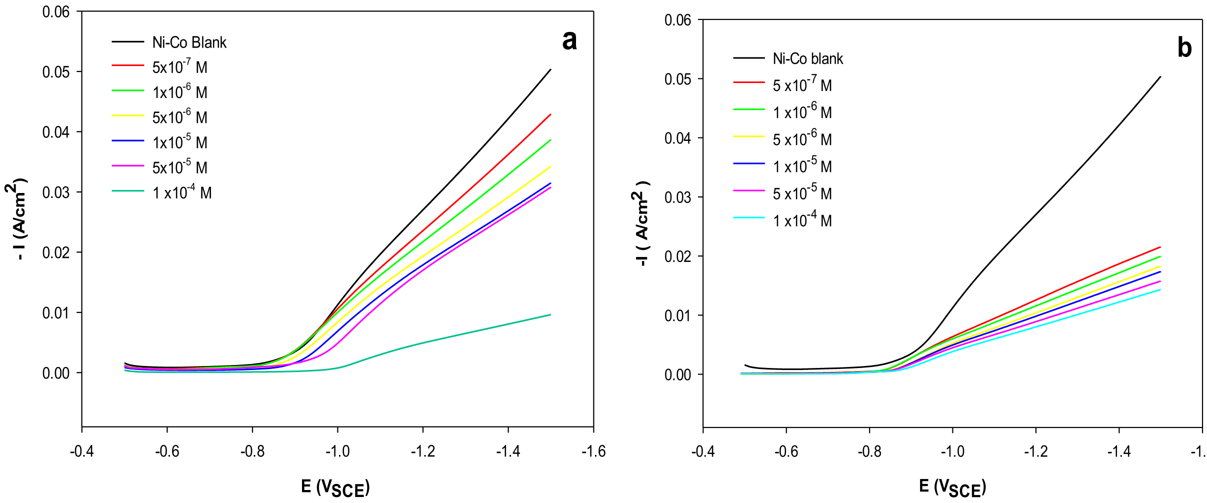

Fig. 4 Potentiodynamic cathodic polarization curves Ni-Co alloy electrodeposition from Ni70%-Co30% bath1 in the absence and presence of different concentrations of (a) [MOFIM]I, (b) [FPIM]Br at pH 4.5.

Table 4 Cathodic polarization potential (CPP) of Ni-Co alloy electrodepositions from bath1 at 5.0×10^{-3} mA cm^{-2} without and with different concentrations of [MOFIM]I and [FPIM]Br and surface coverage (θ) by both ILs at different concentrations.

[MOFIM]I (mol/L)	CPP (V)	θ [MOFIM]I	[FPIM]Br (mol/L)	CPP (V)	θ [FPIM]Br
0.0	−0.93	–	0.0	−0.93	–
5.0×10^{-7}	−0.92	0.13	5.0×10^{-7}	−0.96	0.60
1.0×10^{-6}	−0.93	0.20	1.0×10^{-6}	−0.97	0.64
5.0×10^{-6}	−0.95	0.29	5.0×10^{-6}	−0.99	0.67
1.0×10^{-5}	−0.96	0.34	1.0×10^{-5}	−1.00	0.69
5.0×10^{-5}	−1.01	0.36	5.0×10^{-5}	−1.03	0.72
1.0×10^{-4}	−1.21	0.81	1.0×10^{-4}	−1.06	0.74

Table 5 Tafel slope and kinetic parameters obtained for Ni-Co alloy electrodepositions from bath1 without and with different concentrations of [MOFIM]I and [FPIM]Br.

[MOFIM]I (M)	b_c (mV decade^{-1})	i_c (A cm^{-2})	α_c	[FPIM]Br (M)	b_c (mV decade^{-1})	i_o (Acm^{-2})	α_c
0	−278.4	6.16×10^{-3}	0.04611	0	−278.4	6.16×10^{-3}	0.04611
5×10^{-7}	−307.1	4.75×10^{-3}	0.04302	5×10^{-7}	−325.6	2.35×10^{-3}	0.03943
1×10^{-6}	−298.4	4.16×10^{-3}	0.0180	1×10^{-6}	−323.8	1.99×10^{-3}	0.03823
5×10^{-6}	−291.2	4.41×10^{-3}	0.04408	5×10^{-6}	−335.8	2.08×10^{-3}	0.03965
1×10^{-5}	−261.0	5.53×10^{-3}	0.04918	1×10^{-5}	−335.8	1.99×10^{-3}	0.03823
5×10^{-5}	−206.0	8.99×10^{-3}	0.06232	5×10^{-5}	−323.8	1.85×10^{-3}	0.03965
1×10^{-4}	−143.1	1.02×10^{-2}	0.08971	1×10^{-4}	−306.0	2.09×10^{-3}	0.04195

centrations of studied ILs increased, the i_c appreciably decreased. Generally, the current density decreases when the electrochemical reaction is inhibited (Ibrahim and Al Radadi, 2020; Ibrahim and Omar, 2013). This finding implies that [MOFIM]I and [FPIM]Br inhibit the rate of Co^{2+} and Ni^{2+} transfer across the electrical double layer. The inhibitory effect of the ILs could be due to the cations adsorbing to energetically favored sites of the metal electrode, thus leaving only the high energy surfaces available for deposition on the metal surface (Hashemi et al., 2017). The presence of an adsorbate altered the double layer structure and decreased the rate of the electrochemical reaction (Ibrahim and Omar, 2013; El Sayed and Ibrahim, 2019; Zhang and Hua, 2012). [FPIM]Br showed a stronger decrease in i_c values than [MOFIM]I; this higher inhibition effect of [FPIM]Br on the Ni-Co alloy is supported by the higher polarization shift toward a more negative overpotential, higher CPP values, and more significant drop in the cathodic current.

3.5. Adsorption isotherms

The [MOFIM]I and [FPIM]Br cations are thought to adsorb on the cathode surface. This phenomenon increased the deposition overpotential by decreasing the sites available for the discharge of Co^{2+} and Ni^{2+} during Ni-Co alloy deposition from bath1 with different concentrations of both ILs (Fig. 4). The surface coverage (θ) of the studied ILs was estimated as a constant potential (−1.3 V_{SCE}), as reported in (Ibrahim and Omar, 2013). The θ values by [FPIM]Br were higher than those from [MOFIM]I, as shown in Table 4, which indicates a greater adsorption rate of [FPIM]Br molecules on the cathode surface. However, at 1×10^{-4} M [MOFIM]I, θ recorded the highest value, 0.8105, which means [MOFIM]I cations adsorbed stronger than [FPIM]Br cations. The data were fitted to the Langmuir adsorption isotherm (Ibrahim and Omar, 2013). From Fig. 5, the calculated equilibrium constant values, K, were 33681.14 M^{-1} and 7502.05 M^{-1} for [MOFIM]I and [FPIM]Br adsorption, respectively, from the Ni-Co alloys deposited from baths 2 and 3. A larger K value indicates higher adsorption of the [MOFIM]I compound than the [FPIM]Br compound, i.e., a stronger electrical interactions exist between the double layer at the phase boundary and [MOFIM]I molecules than the boundary and [FPIM]Br molecules.

A spontaneous process for the adsorption of [MOFIM]I molecules on the surface of Cu was indicated by the negative value of $\Delta G°_a$. The calculated $\Delta G°_a$ values of [MOFIM]I and [FPIM]Br are −35.72 and − 32.01 kJ mol^{-1}, respectively, which are between the values for physical (−20 kJ mol^{-1}) and chemical adsorption (−40 kJ mol^{-1}). These results indicate that the adsorption of [MOFIM]I and [FPIM]Br onto the Cu substrate surface involves both chemical and physical adsorption (i.e., mixed type) (Gholami et al., 2013).

3.6. Cyclic voltammetry

Cyclic voltammetry measurements were carried out on a GCE for Ni-Co alloy electrodeposition from baths 1, 2 and 3 with-

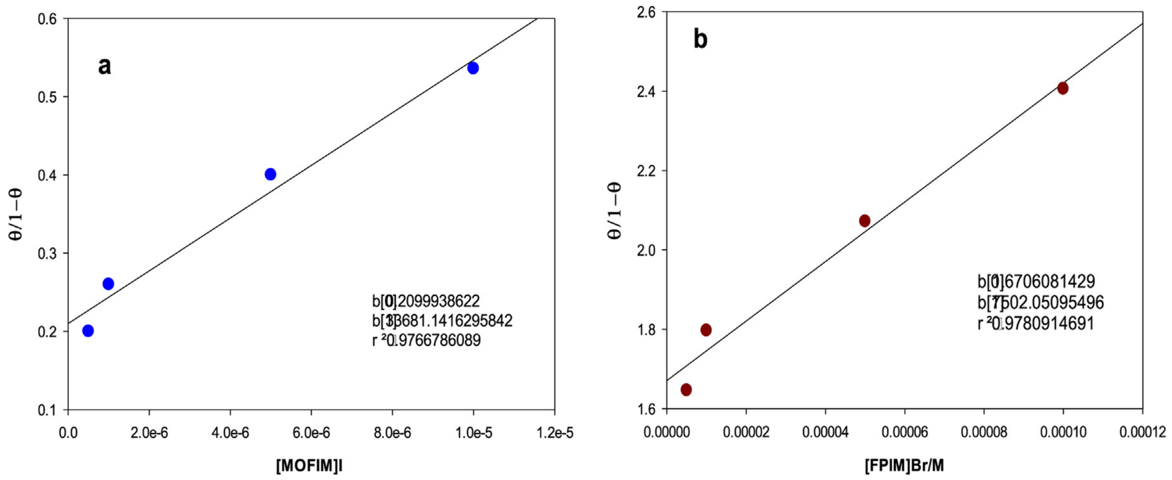

Fig. 5 Plot of θ/(1-θ) vs concentration of (a) [MOFIM]I, (b) [FPIM]Br in Ni-Co alloy electrodeposition from Ni70%-Co30% bath1.

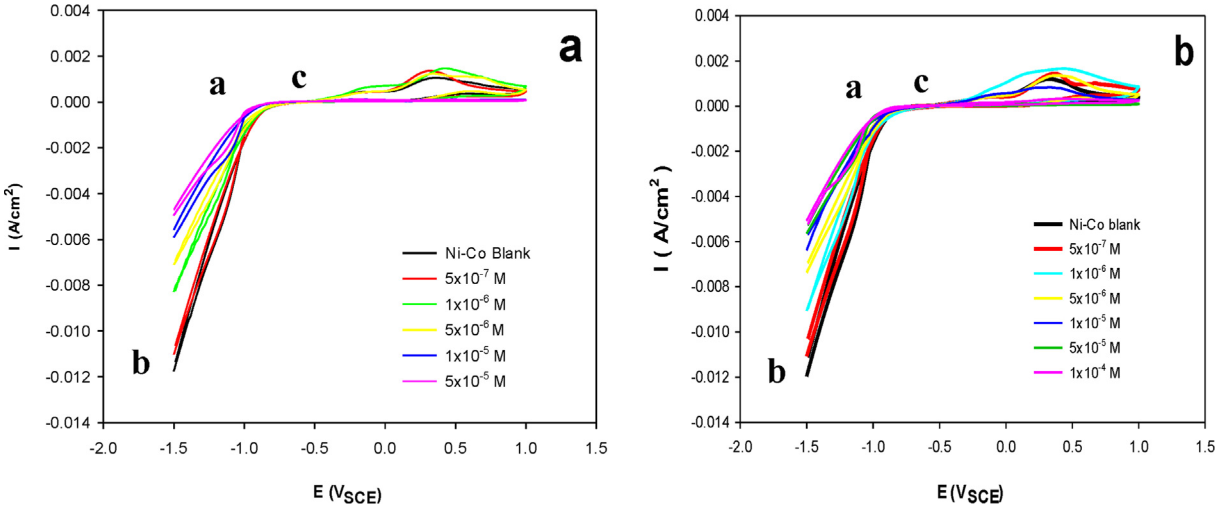

Fig. 6 CVs for Ni-Co alloy electrodeposition from Ni70%-Co30% bath1 at GCE in absence and presence of different concentrations of (a) [MOFIM]I; (b) [FPIM]Br from acidic baths at scan rate of 100 mV/sec.

out and with [MOFIM]I and [FPIM]Br (Fig. 6a, b). The presence of [MOFIM]I and [FPIM]Br in the range 5×10^{-7}--1×10^{-4} M shifted the deposition of the cathodic overpotential to more negative values and inhibited Ni^{2+} and Co^{2+} ion deposition. This behavior is due to the adsorption of the two studied ILs at low energy active sites, thus leaving high energy sites for metal deposition, as confirmed via the cathodic polarization curves. A similar behavior of additives was reported for Ni (Oliveira et al., 2018; Abebe et al., 2013) and Zn electrodeposition (Ibrahim and Omar, 2013; Ibrahim and Messali, 2011). For anodic regain, the height of the anodic oxidation peak decreased with increasing concentration of the studied ILs in solution, and the peak became very broad. The obvious broadening of the oxidation peak for the Ni-Co baths could be explained as a result of the slow dissolution of Ni and Co from the deposited alloy, as reported in (Al Raddadi, 2014). The stripping potential is not observed for Co or Ni in Fig. 6a, b, which suggests that the formulated electrolyte for the Ni-Co alloy forms in the alloy phase only. Similar results were reported in (Vijayakumar et al., 2013). The higher nucleation overpotential (NOP) values in the presence of a high concentration of [MOFIM]I, 1×10^{-5} M and 5×10^{-5} M, as shown in Table 6, indicate stronger polarization (Sorour et al., 2017).

The effect of the scan rates on Ni-Co alloy electrodeposition from bath1 in the presence of [MOFIM]I and [FPIM]Br is shown in Fig. 7a, b. As expected, the increase in the scan rate shifts the alloy reduction peaks to more negative potentials and produces a higher current contribution, which explains why the electrodeposition behavior is qualitatively affected by the scan rate. A current crossover also occurred in the cathodic branches when the nucleation overpotential increased with the scan rate, indicating a typical nucleation process for deposition. For a diffusion-controlled system, the Randles-Sevcik equation (Saha et al., 2014) best describes the electrochemical behavior of an irreversible process. The linear relation between i_{cp} and $v^{1/2}$, as shown in Fig. 7a, b, suggests that the rate of growth is controlled by the mass transfer of Co^{2+} and Ni^{2+} to the growing center. Similar electrochemical results have been reported for Co^{2+} in the reverse micellar

Table 6 NOP of CV measurements and the height of anodic peaks, i_a, of ALSV measurements for Ni-Co alloy electrodeposition from bath1 without and with different concentrations of [MOFIM]I and [FPIM]Br.

[MOFIM]I (M)	NOP (mV)	i_a peek (A cm^{-2})	[FPIM]Br (M)	NOP (mV)	i_a peek (A cm^{-2})
0	0.8400	8.347×10^{-3}	0	0.8400	8.347×10^{-3}
5×10^{-7}	0.8414	4.251×10^{-3}	5×10^{-7}	0.9066	3.667×10^{-3}
1×10^{-6}	0.9097	2.337×10^{-3}	1×10^{-6}	0.9215	3.502×10^{-3}
5×10^{-6}	0.9299	1.344×10^{-3}	5×10^{-6}	0.9365	2.626×10^{-3}
1×10^{-5}	1.0069	9.313×10^{-3}	1×10^{-5}	0.9287	1.140×10^{-3}
5×10^{-5}	1.0576	1.15×10^{-2}	5×10^{-5}	0.9585	6.352×10^{-4}
1×10^{-4}	–	2.25×10^{-2}	1×10^{-4}	0.9585	2.949×10^{-4}

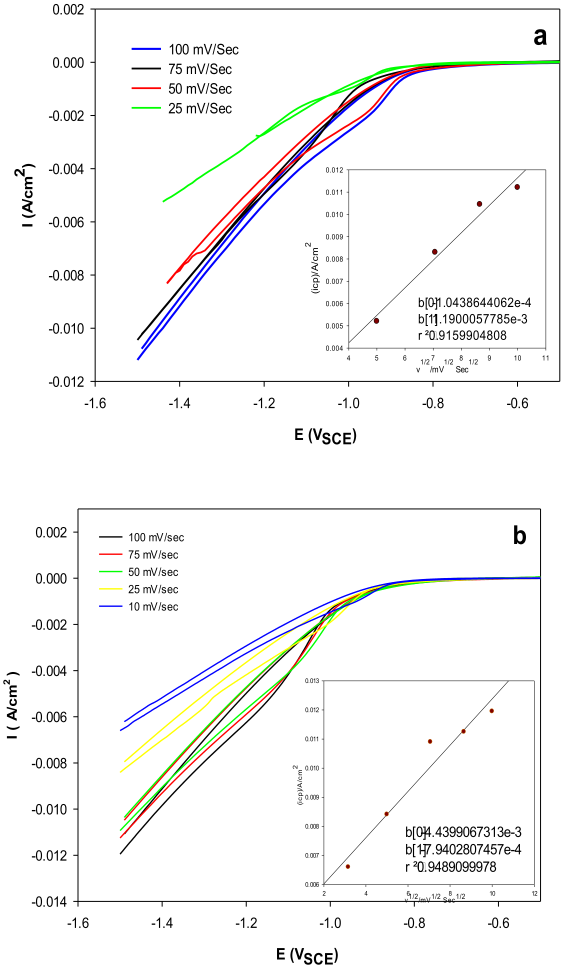

Fig. 7 CVs of Ni-Co alloy electrodeposition recorded at GCE from Ni70%-Co30% bath1 in presence of 5×10^{-7} M (a) [MOFIM]I, (b) [FPIM]Br with different scan rates. Insert linear relation between i_{cp} as a function of the scan potential rate $v^{1/2}$.

solution (Saha et al., 2014), for Zn in the presence of ninhydrin as an organic additive (Ibrahim and Omar, 2013), for 1-butyl-3-methylpyridinium bromide [BMPy]Br with an ionic liquid additive (Ibrahim and Messali, 2011), and for a brass alloy in an ammonia bath (Ibrahim and Bakdash, 2015).

3.7. *In Situ-Anodic linear stripping voltammetry (ALSV)*

As shown in Fig. 8a, b, the ALSVs of the Ni-Co alloy deposited from the bath with a composition of [Ni^{2+}] = 70 g/L and [Co^{2+}] = 30 g/L without and with different concentrations of [MOFIM]I and [FPIM]Br only had one oxidation peak, which resulted from the oxidation of the Ni-Co alloy only that had been previously potentiostatically deposited on the GCE. The presence of a single anodic peak of alloy stripping denotes that the alloy consisted of one phase. Visual observation of the GCE after reaching the anodic peak did not show any residual Ni or Co. Therefore, the charge used through the anodic stripping could be taken as an estimation method for the current efficiency of the Ni-Co alloy depositions. i.e., the area under the peak is equivalent to the amount of alloy deposited. From Fig. 8a, b and Table 6, it is clear that the stripping current, i_a(Acm^{-2}) and the area under the stripping peak were greatly suppressed as the [MOFIM]I and [FPIM]Br concentrations increased from 5×10^{-7} M to 5×10^{-6} M. This finding indicate that the ILs act as inhibitors of Ni-Co alloy deposition. These results agree well with the previous data of the polarization of CVs. However, at higher [MOFIM]I concentrations, from 1×10^{-5} M to 1×10^{-4} M, the stripping peaks and the area under the peaks became significantly more prominent. This finding indicates the rate of alloy deposition, as well as hydrogen evolution, increases. The increase of hydrogen evolution was due to adsorbed [MOFIM]I ions on both the Ni-Co alloy and the Cu substrate, which means the alloy deposition was accelerated at a high [MOFIM]I concentration. A similar behavior was observed during the electrodeposition of Ni and Zn in the presence of Natural Kermes Dye and copper as an additive and impurity, respectively (El Sayed and Ibrahim, 2019; Zhang and Hua, 2012). However, it is obvious that the anodic peaks of the Ni-Co alloy in the presence of [FPIM]Br are lower than in the presence of [MOFIM]I, which confirms the small amount of the Ni-Co alloy deposited on the GCE, as reported in (Abd El Rehim et al., 2002). The easier oxidation of the Ni-Co alloy deposited in the presence of [FPIM]Br leads the potential to shift in a less noble direction. The opposite behavior of the stripping potential for the Ni-Co alloy deposited in the presence of [MOFIM]I is due to the difficulty of the Ni-Co alloy to dissolve. This result agrees with (El Boraei and Ibrahim, 2018).

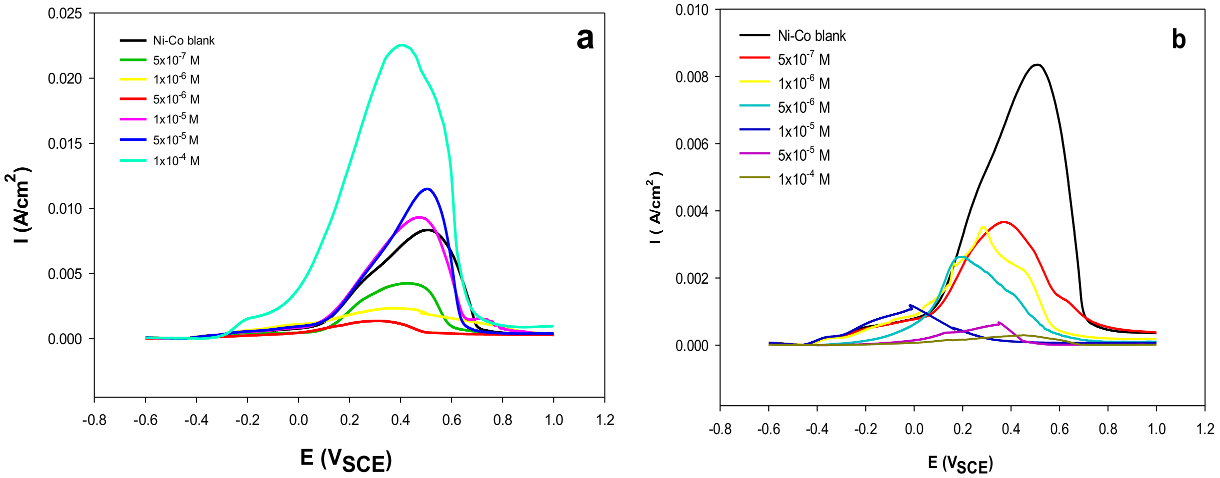

Fig. 8 ALSVs for Ni-Co alloy electrodeposition from Ni70%-Co30% bath1 in absence and presence of different concentrations of (a) [MOFIM]I, (b) [FPIM]Br.

Table 7 The differences between the molecular structures of two ionic liquid imidazole additives during electrodeposition to Ni, Co and Ni-Co alloy.

Differences	[MOFIM]I	[FPIM]Br
Phenyl ring	one	two
Fluorine atom	4 in phenyl ring	1 in phenyl ring
Oxygen atom	1 with amide function group	1 with ether function group
Nitrogen atom	2 with imidazole ring 1 with amide function group	2 with imidazole ring
Alkyl	methyl	butyl

3.8. Quantum chemical calculations

Quantum chemical calculations are used as theoretical tools to explain the performance of two IL imidazole derivatives, [MOFIM]I and [FPIM]Br, with respect to their molecular structural properties as additives during electrodeposition of a Ni-Co alloy. As shown in Fig. 1, there are some similarities and differences between the molecular structures of the two studied ILs, which are considered the predictable active sites for adsorption on the cathode surface. The main similarities are the imidazole ring, phenyl ring, fluorine and oxygen atoms in both compounds. However, many differences are illustrated in Table 7. Moreover, there is a positive charge on one nitrogen atom in the imidazole ring in the cationic form.

The optimized geometries of the molecular structures of the studied ILs in the neutral and cationic forms as estimated by DFT are as shown in Fig. 9. The quantum chemical parameters of both forms are listed in Table 8, including the IE $_{Rct}$ (%) of the Ni-Co2 and Ni-Co3 alloy deposited from bath2 and 3 in the presence of [MOFIM]I and [FPIM]Br. The inhibitory effect of the studied ILs can be attributed to their parallel adsorption on the surface of the Cu substrate. The parallel adsorption of these molecules is attributed to the presence of more than one active center for adsorption. The active centers in the [MOFIM]I and [FPIM]Br chemical structures are as follows:

- The imidazole ring consists of two nitrogen atoms as heteroatoms that have a lone pair of electrons and 4 π-electrons of two conjugated double bonds in both [MOFIM]I and [FPIM]Br.
- Six π-electrons of three conjugated double bonds in the phenyl ring of the ionic liquid [MOFIM]I, and six π-electrons of three conjugated double bonds in the benzyl ring and in the phenoxy ring of [FPIM]Br (12 π-electrons).
- The amide functional group in [MOFIM]I, which has two π-electrons of one double bond as well as nitrogen and oxygen heteroatoms with one and two lone pair electrons. However, the chemical structures of the ionic liquid [FPIM]Br only has one oxygen atom with two lone pair electrons in the phenoxy functional group.
- Three fluorine atoms as heteroatoms contain nine lone pair electrons in the phenyl group in [MOFIM]I and only one fluorine atom with three lone pair electrons in the benzyl group in [FPIM]Br.

In general, as the number of double bonds increases, the number of π-electrons increases and adsorption on the cathode surface becomes easier (Deng et al., 2018). As Ni-Co alloy plating ionic liquid additives, [MOFIM]I and [FPIM]Br with 6 and 12 π-electrons, respectively, can be better adsorbed on the cathode surface and can consequently increase the polarization of the Ni-Co alloy electroplating the most. Moreover, oxygen atoms have the property of electron donation, which is associated with a strong adsorption ability on the surface of metal (Kumar et al., 2019). The nitrogen atoms among the nitrogen heterocyclic compounds were preferred active sites for accepting electrons from the Cu substrate (Ren et al., 2015).

The localization of HOMO and LUMO on the neutral and cation species of both [MOFIM]I and [FPIM]Br are shown in Fig. 10. Based on the studies of the bonding reactions and cloud distributions of the organics, the crimson and green

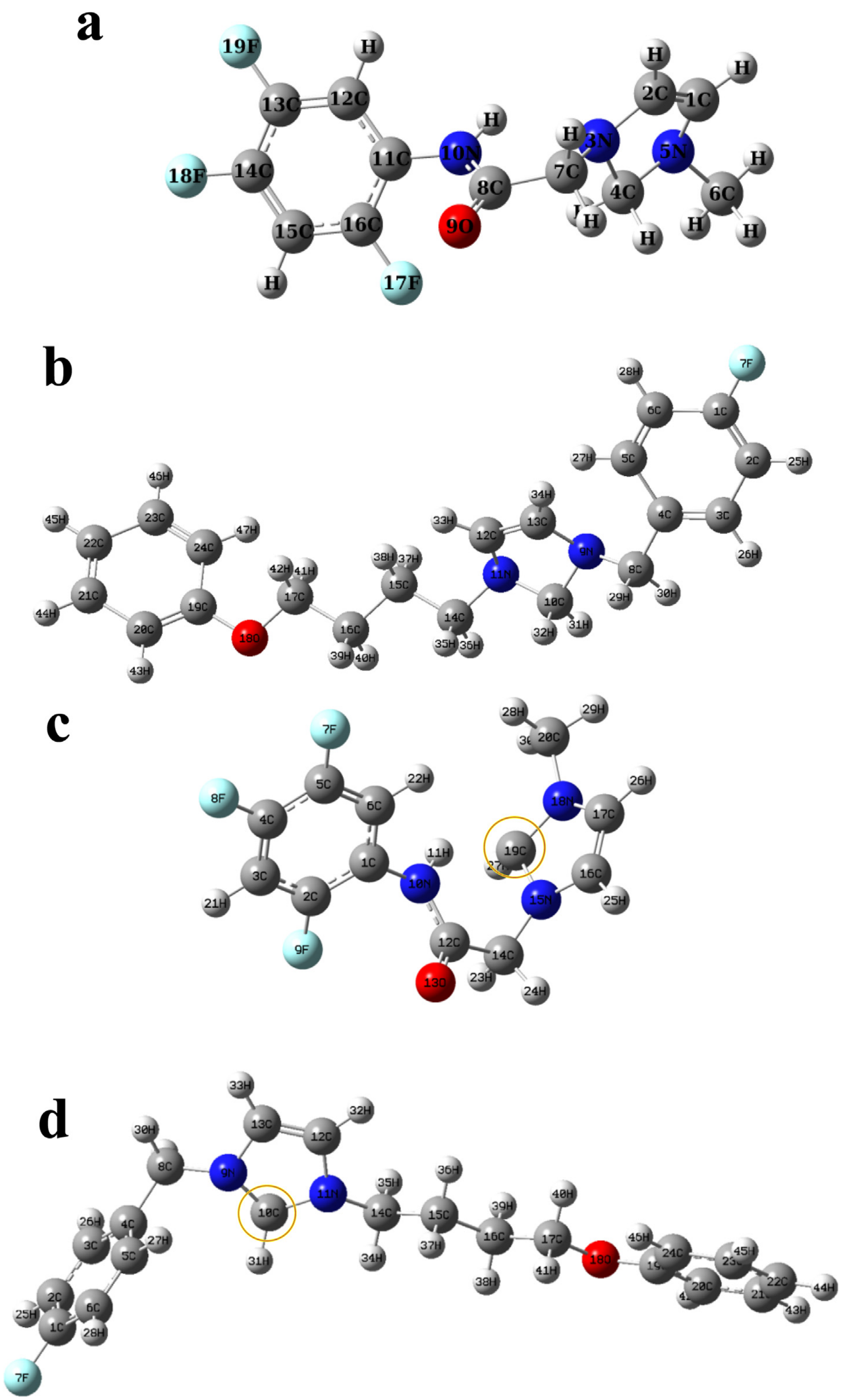

Fig. 9 The optimized molecular structures of (a) [MOFIM]I neutral species, (b) [FPIM]Br neutral species, (c) [MOFIM]I cation species, (d) [FPIM]Br cation species.

color clouds correspond to the phase of orbital wave functions in which one is for the negative phase and the other is for the positive phase (Kumar et al., 2019; Ren et al., 2015). For the two molecules in the neutral form, as illustrated in Fig. 10a, b, a significant electron density of HOMO was localized principally on the imidazole ring of both ILs molecules, which indicates that the characteristic functional group of imidazole and the double bonds in the ring could be electron donors. These sites are the preferred active sites that donate electrons to unoccupied orbitals of Cu atoms. However, Fig. 10a' shows

Table 8 Quantum chemical parameters of neutral and cation species of [MOFIM]I and [FPIM]Br IE_{Rct} (%) of Ni-Co2 and Ni-Co3 alloys.

Quantum parameter	Neutral species		Cation species	
	[MOFIM]I	[FPIM]Br	$[MOFIM]^+$	$[FPIM]^+$
E_{HOMO} (eV)	−0.19396	**−0.18008**	−0.24215	**−0.22475**
E_{LUMO} (eV)	**−0.04944**	−0.03253	**−0.05447**	−0.03365
ΔE (eV)	**0.14452**	0.14755	**0.18768**	0.19110
I (eV)	0.19396	0.18008	0.24215	0.22475
A (eV)	0.04944	0.03253	0.05447	0.03365
χ (eV)	0.12170	0.10630	0.14831	0.12920
η (eV)	**0.07226**	0.07377	**0.09384**	0.09555
S	**13.8389**	13.5547	**10.6564**	10.4657
ΔN	**0.84209**	0.72046	**0.79022**	0.67608
IE_{Rct} (%)	53.05	44.33	53.05	44.33

that a significant electron density of HOMO in the cation form of [MOFIM]I is localized principally on the phenyl ring and the amide functional group, which indicates that 6 π-electrons, F7, F8, and F9 in the phenyl ring and 2 π-electrons, N10, O13, in the amide function group of [MOFIM]I could be the donors of the electron associated with the strong adsorption ability of [MOFIM]I on the surface of metal, i.e., they are the preferred active sites that donate electrons to the unoccupied orbitals of Cu atoms. A distribution of the HOMO electronic density in the [FPIM]Br cation species, Fig. 10b' localized on N9 and N11 and 4 π-electrons of 2 double bonds in the imidazole ring. These results suggest that nitrogen atoms and π electrons are the favorable sites for the strong adsorption of [FPIM]Br on the surface of metals. The LUMO electron density shown in Fig. 10c is distributed over each atom of the tri-fluoro phenyl aromatic ring and the amide group of the [MOFIM]I molecule in neutral form. However, the LUMO electron density is distributed intensely over the imidazole ring in the cation species of the [MOFIM]I molecule, and a thin distribution of LUMO appears on N10, O13 in the amide function group and the C atoms in the phenyl ring of [MOFIM]I, as show in Fig. 10c'. The LUMO electron density is distributed over each carbon atom of the 4-fluorobenzyl aromatic ring in the [FPIM]Br molecule in neutral form (Fig. 10d), indicating it is the site that accepts electrons from Cu atoms to form back-donation bonds. However, LUMO is distributed in the benzyl ring of the [FPIM]Br cation (Fig. 10d'). These results suggest that the acceptor sites of the donated electrons from the cathode surface are the atoms of the imidazole ring and the atoms of the amide function group of [MOFIM]I. The acceptor sites of [FPIM]Br are in the benzyl ring.

It is concluded that the preferred active sites for donating and accepting electrons in the neutral forms of both studied ILs were located within the N, O, and F atoms, which have pairs of electrons, and the rings, which consist of π-electrons. For the cationic forms of both ILs, the preferred active sites for donating and accepting electrons are located on the nitrogen atoms and the aromatic rings. The density distributions of the frontier molecular orbitals (HOMO and LUMO) of the two studied ILs molecules show that the nitrogen atoms and π-electrons are the preferential sites for strong adsorption on the surface of metal. It is worth mentioning that the [MOFIM]I and [FPIM]Br ionic liquids not only provide electrons to the unoccupied d orbital of the metal ion but can also receive an electron from the d orbital of the metal, resulting in the formation of a feedback bond.

According to the frontier molecular orbital theory, the energy of the highest occupied molecular orbital (E_{HOMO}) and the energy of the lowest unoccupied molecular orbital (E_{LUMO}) are often associated with the electron donating and electron accepting abilities of molecules.

E_{HOMO} is associated with the ability of the molecule to donate electrons. Additives with a high E_{HOMO} value tend to donate electrons to vacant orbitals of an appropriate acceptor with lower energy. E_{HOMO} expresses the affinity of a molecule to provide electrons to a proper acceptor molecule with low empty molecular orbital energy (Zohdy et al., 2019). E_{LUMO} is the capacity of a molecule to accept electrons. The affinity for the formation of a feedback bond depends on the value of E_{LUMO}, which eases the acceptance of electrons from the d orbital of the metal (Zohdy et al., 2019). A lower E_{LUMO} indicates a better capacity of additives to accept electrons from the cathode surface. A lower value of $\triangle E$ corresponds to a more stable adsorption layer of IL additives on the surface of metal, which contribute to a stronger inhibition of Ni^{+2} and Co^{+2} composite electrodeposition (Deng et al., 2018).

[FPIM]Br in neutral and cation forms exhibited a higher value of E_{HOMO} than [MOFIM]I, as listed in Table 8. This finding is indicative of the stronger adsorption capacity of [FPIM]Br achieved by donating electrons to the appropriate acceptor molecules with low energy empty molecular orbitals (Kumar et al., 2019). Further, an increased E_{HOMO} value facilitates its effective adsorption on the cathode surface, resulting in its enhanced protection efficiency by influencing the charge transfer process throughout the adsorbed additive layer (Kumar et al., 2019). However, considering only E_{HOMO} is not enough to estimate the inhibition performance of the additives; in fact, organic compounds are considered to be excellent corrosion inhibitors if they can donate and accept electrons to/from the surface of metal (Al-Fakih, 2017). The adsorption of an additive on the surface of a cathode and its inhibition performance can be estimated based on the values of several quantum parameters. Therefore, as show in Table 8, the lower

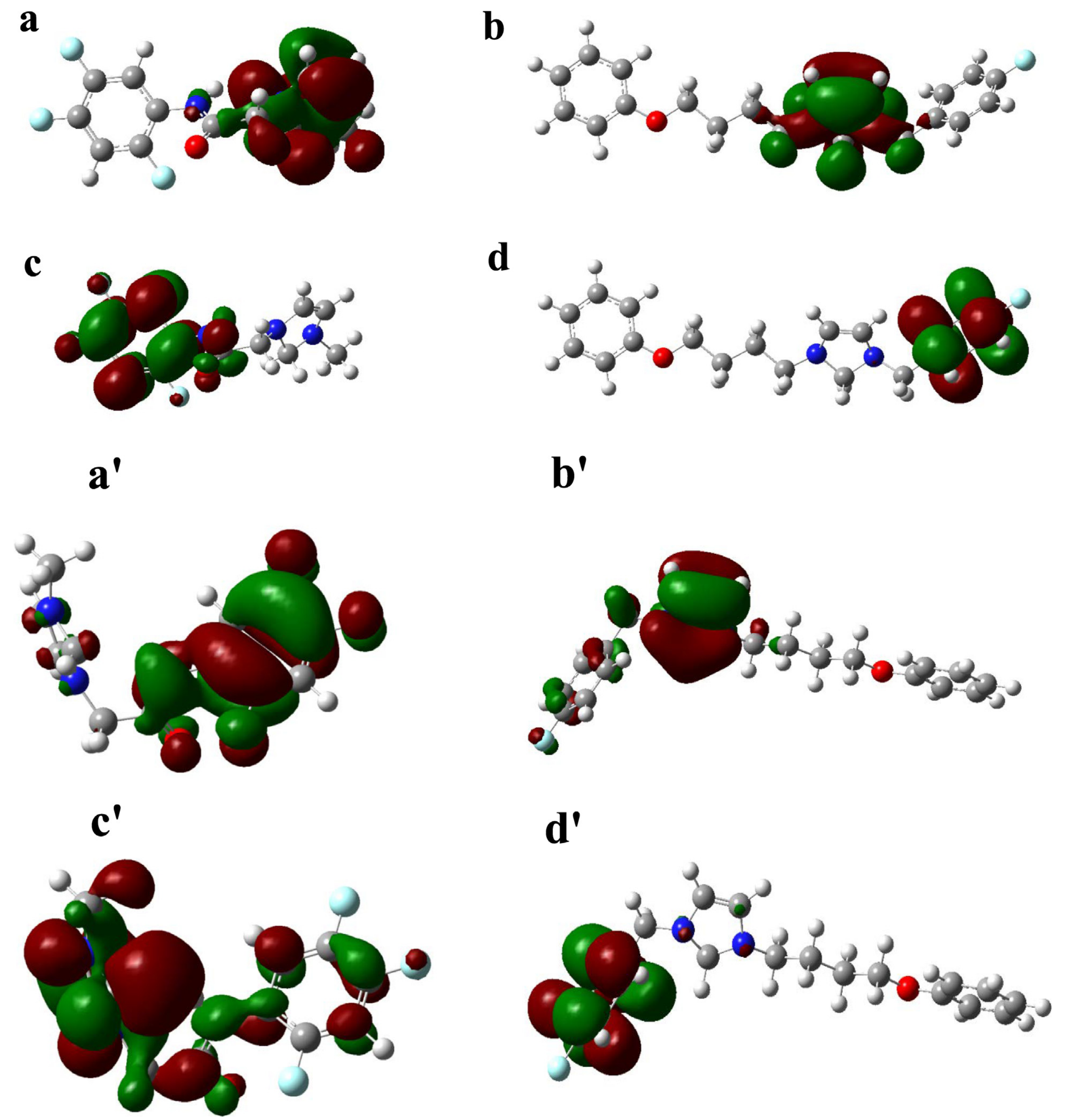

Fig. 10 Localization of HOMO of neutral species (a)[MOFIM]I, (b)[FPIM]Br, LUMO of (c)[MOFIM]I and (d)[FPIM]Br. HOMO of cation form (a')[MOFIM]$^+$, (b')[FPIM]$^+$, LUMO of (c') [MOFIM]$^+$ and (d') [FPIM]$^+$.

values of E_{LUMO} of [MOFIM]I in the neutral, −0.04944 eV, and cationic forms, −0.05447 eV, than the E_{LUMO} values of [FPIM]Br in both forms, −0.03253 eV and −0.03365 eV, respectively, indicate the better probability of the [MOFIM]I molecule to accept electrons, as reported in (Kumar et al., 2019), which results in the stronger adsorption of [MOFIM]I on the deposit surface. In principle, the adsorption capacity of the additive molecules to the metal surface increases with an increase of E_{HOMO} or a decrease of E_{LUMO}, which would produce a stronger additive adsorption on the metal surface (Kumar et al., 2019).

The affinity for the formation of a feedback bond depends on the value of E_{LUMO}, which eases the acceptance of electrons from the d orbital of the metal. In the same way, the smaller ΔE between frontier molecular orbitals of additives molecules shows a stronger adsorption bonding ability and greater adsorption stability (Kumar et al., 2019; Ren et al., 2015) of the additive molecules on the metal or alloy surface. In the current study, the [MOFIM]I molecule and cation have lower ΔE values of 0.14452 eV and 0.18768 eV, respectively, than those of the [FPIM]Br molecule and cation, 0.14755 eV and 0.1911 eV, respectively, as shown in Table 8. These results indicate the stronger and more effective adsorption of [MOFIM]I molecules or cations on the surface of Cu and depicts the greater electron transfers between the molecular orbits. The lower values of E_{LUMO} and ΔE obtained for [MOFIM]I justify its higher inhibition efficiency, IE%, than the [FPIM]Br ionic liquid. Similar results with small ΔE values were reported by using nitrogen heterocyclic compounds (NHCs) as additives in the Cu electrodeposition (Ren et al., 2015).

The HOMO and LUMO energies are linked to I and A, respectively. A high value of I indicates the ability of an inhibitor to donate electrons. A is associated with accepting electrons a high value of A indicates the capability of an additive to accept electrons (Al-Fakih, 2017). Absolute η and S are important properties that measure both the stability and reactivity of inhibitor molecules, respectively. Hard molecules have large energy gaps, and soft molecules have small energy gaps. Soft molecules are more reactive than hard ones because they can easily offer electrons to the acceptor (El-Raouf et al., 2018) (the copper surface in the current study). According to previous studies, adsorption probably occurs at the site of the molecule where S has the highest value to facilitate the transfer of the electrons (Al-Fakih, 2017). The [MOFIM]I ionic liquid had higher I, A and S values in both neutral and cationic forms (Table 8), indicating its better ability to donate and accept electrons and its property as a more efficient additive than that of [FPIM]Br. This finding suggests a higher corrosion inhibition efficiency of [MOFIM]I than [FPIM]Br. These theoretical results are consistent with the experimental data.

The value of ΔN is related to the inhibition efficiency obtained by donating electrons. Whereas a positive value of ΔN suggests electron transfer from molecule to metal, a negative value indicates electron transfer in the reverse direction (Sulaiman et al., 2019). In this work, [MOFIM]I and [FPIM]Br in both neutral and cationic forms have positive values for ΔN in the gas phase, as shown in Table 8, suggesting electron transfer from the molecules to metal. According to Lukovits et al. (2001), if $\Delta N < 3.6$, the inhibition efficiency increases with the increase of the ability to donate electrons to the surface of metal; the ΔN values in Table 8 agree with Lukovits' study. [MOFIM]I in both forms has higher ΔN values, 0.84 eV and 0.79 eV, than [FPIM]Br, 0.72 eV and 0.67 eV, respectively. This result confirms the higher inhibition efficiency of the [MOFIM]I inhibitor.

In conclusion, according to the experimental results, the [MOFIM]I inhibitor shows a better inhibition efficiency than the [FPIM]Br inhibitor in both neutral and cationic forms. The better inhibition performance of [MOFIM]I than [FPIM]Br suggests a higher bonding of [MOFIM]I on the surface of the copper substrate. The quantum calculations at the B3LYP/6-311++G(d,p) basis set level of DFT was used to gain a theoretical description of the inhibition performance of the ionic liquids additives. For the studied additives or inhibitors, the inhibition efficiency is increased by a lower LUMO energy, lower energy gap, higher ionization potential, higher electron affinity, and higher softness. The results obtained by quantum calculations suggest that the corrosion inhibition efficiencies of the studied ionic liquids additives follow the trend: [MOFIM]I > [FPIM]Br. The results obtained by the quantum chemical study are consistent with the experimental findings.

3.9. Natural atomic charge

The adsorption mode and the active sites of the [MOFIM]I and [FPIM]Br ILs additives were investigated based on their molecular structures using quantum chemical calculations.

In the electrodeposition of the Ni-Co alloy, the [MOFIM]I and [FPIM]Br additives can form coordination bonds between the unshared electron pairs of oxygen and nitrogen heteroatoms and the empty orbital of the Cu atoms on the Cu substrate and between the empty 3d orbitals of the Ni and Co atoms on the Ni-Co alloy deposit surfaces. In addition, other atoms of the additives can accept electrons from the Cu atom of the Cu substrate surface to form a back-donating bond. Similar results were reported in (Al-Fakih, 2017).

The natural atomic charges of each atom of the [MOFIM]I and [FPIM]Br molecules and the $[\mathrm{MOFIM}]^+$ and $[\mathrm{FPIM}]^+$ cations are displayed in Tables 9 and 10. The data in both Tables give mechanistic information for the adsorption properties of both studied ILs onto the surface of the Ni-Co alloy. Some atoms of molecules and cations have negative charges, but others have positive charges. The heteroatoms containing electron pairs have negative charges. The higher negative charges of the [MOFIM]I molecule in its neutral form are in the following order: N(10) > O(9), in the imide function group and N(3) > N(5) in the imidazole ring; the charges of the imide group are higher than those of the imidazole ring. In the $[\mathrm{MOFIM}]^+$ cation, the higher negative charges are as follows: N(10) > O(13) in the amide functional group and N (15) > N(18) in imidazole ring; the charges in the amide functional group are higher than those of the imidazole ring (Table 9). These findings indicate that previous atoms have higher abilities to donate electrons compared to other atoms of the studied ILs. The lower negative charges are ordered as F(17) > F(18) > F(19) for [MOFIM]I and as F(7) > F(9) > F(8) for $[\mathrm{MOFIM}]^+$, indicating their lower ability to donate electrons (Table 9). For [FPIM]Br IL, Table 10 shows that the higher negative charges of the natural atomic charges in both species are in the following: O(18), in ether function group, > N(11) > N(9), in imidazole ring, indicating their higher ability to donate electrons. Lower negative charges are shown in the order F(7) > C(16) > C(15) for the [FPIM]Br molecule and in order C(16) > C(15) > F(7) for the $[\mathrm{FPIM}]^+$ cation, indicating their lower ability to donate electrons. These findings clearly denote the electron donating abilities of nitrogen and oxygen atoms to the unoccupied metal atomic orbitals, which act as reactive sites for the effective adsorption (Kumar et al., 2019).

Based on the results above, it can be concluded that the quantum calculations are effective tools to provide theoretical insights into the performance of additives in electrodeposition processes. In addition, the quantum chemical calculations can be used as complements to experimental investigation techniques.

4. Conclusion

The impact of the [MOFIM]I and [FPIM]Br ILs as additives was studied to investigate the corrosion behavior of Ni-Co coelectrodeposition from an acidic sulfate bath with three different $[\mathrm{Ni}^{2+}]$ and $[\mathrm{Co}^{2+}]$ concentrations. The Ni-Co2 and Ni-Co3 alloys exhibited the highest corrosion resistance properties among the nine Ni-Co alloys. The $\mathrm{IE}_{\mathrm{Rct}}\%$ of [MOFIM]I in the

Table 9 The natural atomic charges of each atoms in neutral and cation forms of [MOFIM]I molecule.

Atom number	Neutral form		Cation form	
	Atom	Charge	Atom	Charge
1	C	−0.04571	C	0.09401
2	C	−0.06533	C	0.42323
3	N	−0.56276	C	−0.30438
4	C	0.05049	C	0.36434
5	N	−0.52926	C	0.34577
6	C	−0.35018	C	−0.24171
7	C	−0.24592	F	−0.33540
8	C	0.68009	F	−0.33227
9	O	−0.60565	F	−0.33404
10	N	−0.65766	N	−0.66821
11	C	0.09412	H	0.40944
12	C	−0.24012	C	0.67703
13	C	0.34745	O	−0.60599
14	C	0.36666	C	−0.24286
15	C	−0.30330	N	−0.45829
16	C	0.42247	C	−0.04759
17	F	−0.33492	C	−0.04722
18	F	−0.33070	N	−0.45409
19	F	−0.33408	C	−0.01311
20	H	0.21036	C	−0.34228

Table 10 The natural atomic charges of each atoms in neutral and cation forms of [FPIM]Br molecule.

Atom number	Neutral form		Cation form	
	Atom	Charge	Atom	Charge
1	C	0.40870	C	0.40939
2	C	−0.26178	C	−0.26079
3	C	−0.18079	C	−0.17804
4	C	−0.06421	C	−0.06369
5	C	−0.17387	C	−0.17580
6	C	−0.25811	C	−0.25861
7	F	−0.35624	F	−0.35620
8	C	−0.17051	C	−0.16615
9	N	−0.53775	N	−0.47998
10	C	0.05617	C	0.03635
11	N	−0.53810	N	−0.47520
12	C	−0.06077	C	−0.05872
13	C	−0.06131	C	−0.04579
14	C	−0.15300	C	−0.15156
15	C	−0.38642	C	−0.38711
16	C	−0.39138	C	−0.39188
17	C	−0.01484	C	−0.01477
18	O	−0.55471	O	−0.55435
19	C	0.32482	C	0.32472
20	C	−0.24033	C	−0.24001
21	C	−0.18633	C	−0.18613
22	C	−0.23663	C	−0.23645
23	C	−0.18252	C	−0.18262
24	C	−0.29250	C	−0.29263

Ni-Co2 alloy was higher than that of [FPIM]Br in the Ni-Co3 alloy. Higher inhibition in Ni^{2+} and Co^{2+} reduction is indicated by the increasing shift of the cathodic polarization curves towards more negative potentials, the increasing nucleation over potential (NOV) values in CVs, and the strong suppression of the stripping current peak when the concentration of the studied ILs increases in the bath. The inhibition effect of the [MOFIM]I and [FPIM]Br molecules due to their adsorption on the cathode surface obeys Langmuir adsorption. Compared to [FPIM]Br, [MOFIM]I has lower values of E_{LUMO} and ΔE and higher values of *I, A, S and* ΔN in both neutral and cationic forms, indicating its better corrosion inhibition efficiency and more efficient additive properties. According to the natural atomic charges, [MOFIM]I has the strongest adsorption ability on the Cu substrate and a higher $\mathrm{IE}_{\mathrm{Rct}}\%$ than that of [FPIM]Br. These results show that the theoretical results are consistent with the experimental findings.

Declaration of Competing Interest

The authors declare that they have no known competing financial interests or personal relationships that could have appeared to influence the work reported in this paper.

Acknowledgments

The authors would like to thank Professor Dr. Nadjet Rezki and Dr. Mouslim Messali from chemistry department college of science in Taibah University for their cooperation in preparing [MOFIM]I and [FPIM]Br ionic liquids. The authors also like to thank laboratory technicians Abdoulah Jaber from physic department and Fatimah Abdolraheem and Roaa Abosaif from chemistry department faculty of science in Taibah University for their cooperation in all characterization analysis.

Appendix A. Supplementary material

Supplementary data to this article can be found online at https://doi.org/10.1016/j.arabjc.2020.11.015.

References

Abd El Rehim, S.S., Ibrahim, M.A.M., Dankeria, M.M., Emad, M., 2002. Electrodeposition of amorphous cobalt-manganese alloys on to steel from gluconate baths. Trans. IMF 80 (3), 105–109.

Abebe, A., Admassie, S., Villar-Garcia, I.J., Chebude, Y., 2013. 4, 4-Bipyridinium ionic liquids exhibiting excellent solubility for metal salts: Potential solvents for electrodeposition. Inorg. Chem. Commun. 29, 210–212.

Al Radadi, R.M., Ibrahim, M.A.M., 2020. Nickel-cobalt alloy coatings prepared by electrodeposition Part I: Cathodic current efficiency, alloy composition, polarization behavior and throwing power. Korean J. Chem. Eng. 37 (2), 1–10.

Al Raddadi, R.M., 2014. Cathodic codeposition of nickel-cobalt alloy coatings from acidic glycine complex baths MS thesis. Taibah University, Faculty of Science.

Alesary, H.F., Cihangir, S., Ballantyne, A.D., Harris, R.C., Weston, D.P., Abbott, A.P., Ryder, S.R., 2019. Influence of additives on the electrodeposition of zinc from a deep eutectic solvent. Electrochim. Acta 304, 118–130.

Al-Fakih, A.M.A., 2017. Experimental and computational studies of furan derivatives in corrosion inhibition of mild steel PhD thesis. Universiti Teknologi Malaysia, Faculty of Science.

Al-Fakih, A.M., Abdallah, H.H., Aziz, M., 2019. Experimental and theoretical studies of the inhibition performance of two furan derivatives on mild steel corrosion in acidic medium. Mater. Corros. 70 (1), 135–148.

Anicai, L., Sin, I., Brincoveanu, O., Costovici, S., Cotarta, A., Cojocaru, A., Enachescu, M., Visan, T., 2019. Electrodeposition of lead selenide films from ionic liquids based on choline chloride. Appl. Surf. Sci. 475, 803–812.

Bakkar, A., Neubert, V., 2020. Electrodeposition of photovoltaic thin films from ionic liquids in ambient atmosphere: Gallium from a chloroaluminate ionic liquid. J. Electroanal. Chem. 856, 113656–113663.

Belghiti, M.E., Bouazama, S., Echihi, S., Elmelouky, A., Dafali, A., Emran, K.M., Hammouti, B., Tabyaoui, M., 2020. Understanding the adsorption of newly Benzylidene-aniline derivatives as a corrosion inhibitor for carbon steel in hydrochloric acid solution: Experimental, DFT and molecular dynamic simulation studies. Arab. J. Chem. 13 (1), 1499–1519.

Bouoidina, A., El-Hajjaji, F., Emran, K., Belghiti, M.E., Elmelouky, A., Taleb, M., Abdellaoui, A., Hammouti, B., Obot, I.B., 2019. Towards understanding the anticorrosive mechanism of novel surfactant based on Mentha pulegium oil as eco-friendly bio-source of mild steel in acid medium. Chem. Res. Chinese Univ. 35 (1), 85–100.

Carlesi, C., Cortes, E., Dibernardi, G., Morales, J., Muñoz, E., 2016. Ionic liquids as additives for acid leaching of copper from sulfidic ores. Hydrometallurgy 161, 29–33.

Chai, Z., Jiang, C., 2019. Electrochemical/chemical growth of porous (Ni Co, Cu)(OH) 2 as an electrode material: Ternary Ni-Co-Cu nanocrystalline films corroded in neutral salt spray. Electrochim. Acta 294, 11–21.

Deng, J., Zhang, J., Tu, Y., Yang, P., An, M., Wang, P., 2018. Effect of BEO in the electrodeposition process of Ni/diamond composite coatings for preparation of ultra-thin dicing blades: Experiments and theoretical calculations. Ceram. Int. 44 (14), 16828–16836.

El Adnani, Z., Mcharfi, M., Sfaira, M., Benzakour, M., Benjelloun, A. T., Emran, K.M., 2020. Reactivity and Fe complexation analysis of a series of quinoxaline derivatives used as steel corrosion inhibitors. Struct. Chem. 31 (2), 631–645.

El Boraei, N.F., Ibrahim, M.A.M., 2018. Catalytic effect of l-proline on the reduction of Ni (II) ions during nickel electrodeposition from a Watts-type nickel bath. Surf. Coatings Technol. 347, 113–122.

El Sayed, M.A., Ibrahim, M.A.M., 2019. Natural kermes dye as an effective additive for electrochemical deposition of nickel from watts-type nickel bath. Int. J. Electrochem. Sci. 14, 4957–4973.

El-Raouf, M.A., Khamis, E.A., Kana, M.T.H.A., Negm, N.A., 2018. Electrochemical and quantum chemical evaluation of new bis (coumarins) derivatives as corrosion inhibitors for carbon steel corrosion in 0.5 M H2SO4. J. Mol. Liq. 255, 341–353.

Frisch, M.J., Trucks, G.W., Schlegel, H.B., Scuseria, G.E., Robb, M. A., Cheeseman, J.R., Scalmani, G., Barone, V., Mennucci, B., Petersson, G.A., Nakatsuji, H., Caricato, M., Li, X., Hratchian, H. P., Izmaylov, A.F., Bloino, J., Zheng, G., Sonnenberg, J.L., Hada, M., Ehara, M., Toyota, K., Fukuda, R., Hasegawa, J., Ishida, M., Nakajima, T., Honda, Y., Kitao, O., Nakai, H., Vreven, T., Montgomery Jr., J.A., Peralta, J.E., Ogliaro, F., Bearpark, M., Heyd, J.J., Brothers, E., Kudin, K.N., Staroverov, V.N., Kobayashi, R., Normand, J., Raghavachari, K., Rendell, A., Burant, J.C., Iyengar, S.S., Tomasi, J., Cossi, M., Rega, N., Millam, J.M., Klene, M., Knox, J.E., Cross, J.B., Bakken, V., Adamo, C., Jaramillo, J., Gomperts, R., Stratmann, R.E., Yazyev, O., Austin, A.J., Cammi, R., Pomelli, C., Ochterski, J.W., Martin, R.L., Morokuma, K., Zakrzewski, V.G., Voth, G.A., Salvador, P., Dannenberg, J.J., Dapprich, S., Daniels, A.D., Farkas, O., Foresman, J.B., Ortiz, J. V., Cioslowski, J., Fox, D.J., 2009. Gaussian 09, Revision B.1. Gaussian Inc., Wallingford CT.

Gholami, M., Danaee, I., Maddahy, M.H., RashvandAvei, M., 2013. Correlated ab initio and electroanalytical study on inhibition behavior of 2-mercaptobenzothiazole and its thiole–thione tautomerism effect for the corrosion of steel (API 5L X52) in sulphuric acid solution. Ind. Eng. Chem. Res. 52 (42), 14875–14889.

Hashemi, A.B., Kasiri, G., La Mantia, F., 2017. The effect of polyethyleneimine as an electrolyte additive on zinc electrodeposition mechanism in aqueous zinc-ion batteries. Electrochim. Acta 258, 703–708.

Ibrahim, M.A.M., Al Radadi, R.M., 2020. Nickel-cobalt alloy coatings prepared by electrodeposition Part II: Morphology, structure, microhardness, and electrochemical studies. Korean J. Chem. Eng., 1–11 https://doi.org/10.1007/s11814-020-0661-8.

Ibrahim, M.A., Bakdash, R.S., 2015. New cyanide-free ammonia bath for brass alloy coatings on steel substrate by electrodeposition. Int. J. Electrochem. Sci. 10, 9666–9677.

Ibrahim, S., Bakkar, A., Ahmed, E., Selim, A., 2016. Effect of additives and current mode on zinc electrodeposition from deep eutectic ionic liquids. Electrochim. Acta 191, 724–732.

Ibrahim, M.A.M., Messali, M., 2011. Ionic Liquid [BMPy] Br as an effective additive auring Zinc electrodeposition from an aqueous Sulfate bath. Prod. Finish 2, 182–190.

Ibrahim, M.A.M., Omar, E.M.A., 2013. Synergistic effect of ninhydrin and iodide ions during electrodeposition of zinc at steel electrodes. Surf. Coatings Technol. 226, 7–16.

Jiang, Q.S., Cheng, W., Li, W., Yang, Z., Zhang, Y., Ji, R., Yang, X., Ju, Y., Yu, Y., 2019. One-step electrodeposition of amorphous nickel cobalt sulfides on FTO for high-efficiency dye-sensitized solar cells. Mater. Res. Bull. 114, 10–17.

Pramod Kumar, U., Shanmugan, S., Joseph Kennady, C., Shibli, S.M. A., 2019. Anti-corrosion and microstructural properties of Ni–W alloy coatings: effect of 3, 4-Dihydroxybenzaldehyde. Heliyon 5, (3) e01288.

Lallemand, F., Comte, D., Ricq, L., Renaux, P., Pagetti, J., Dieppedale, C., Gaud, P., 2004. Effects of organic additives on electroplated soft magnetic CoFeCr films. Appl. Surf. Sci. 225 (1–4), 59–71.

Lokhande, A.C., Bagi, J.S., 2014. Studies on enhancement of surface mechanical properties of electrodeposited Ni–Co alloy coatings due to saccharin additive. Surf. Coatings Technol. 258, 225–231.

Lukovits, I., Kalman, E., Zucchi, F., 2001. Corrosion inhibitors—correlation between electronic structure and efficiency. Corrosion 57 (1), 3–8.

Murulana, L.C., Kabanda, M.M., Ebenso, E.E., 2016. Investigation of the adsorption characteristics of some selected sulphonamide derivatives as corrosion inhibitors at mild steel/hydrochloric acid interface: Experimental, quantum chemical and QSAR studies. J. Mol. Liq. 215, 763–779.

Oliveira, R.P., Bertagnolli, D.C., Ferreira, E.A., da Silva, L., Paula, A. S., 2018. Influence of Fe2+ oxidation and its antioxidant ascorbic acid as additive in Zn-Ni-Fe electrodeposition process on a low carbon steel. Surf. Coatings Technol. 349, 874–884.

Omar, I.M.A., Aziz, M., Emran, K.M., 2020. Part I: Ni-Co alloy foils electrodeposited using ionic liquids. Arab J Chem 13 (11), 7707–7719.

Omar, I.M.A., Aziz, M., Emran, K.M., 2020. Impact of Ionic Liquid [FPIM]Br on Electrodeposition of Ni and Co from Aqueous Sulfate Bath (submitted for publication).

Qibo, Z., Yixin, H., 2017. Ionic liquids as electrodeposition additives and corrosion inhibitors. Progress and Developments in Ionic Liquids. InTech.

Rahmani, H., Ismaily Alaoui, K., Emran, K.M., El Hallaoui, A., Taleb, M., El Hajji, S., Labriti, B., Ech-chihbi, E., Hammouti, B., El-Hajjaji, 2018. Experimental and DFT Investigation on the Corrosion Inhibition of Mild Steel by 1, 2, 3-Triazolereg Ioisomers in 1M Hydrochloric Acid Solution. Preprints (www.preprints.org). https://doi.org/10.20944/preprints201803.0116.v1.

Ren, S., Lei, Z., Wang, Z., 2015. Investigation of nitrogen heterocyclic compounds as levelers for electroplating cu filling by electrochemical method and quantum chemical calculation. J. Electrochem. Soc. 162 (10), D509–D514.

Ren, X., Song, Y., Liu, A., Zhang, J., Yuan, G., Yang, P., Zhang, J., An, M., Matera, D., Wu, G., 2015. Computational chemistry and electrochemical studies of adsorption behavior of organic additives during gold deposition in cyanide-free electrolytes. Electrochim. Acta 176, 10–17.

Rezki, N., Al-blewi, F.F., Al-Sodies, S.A., Alnuzha, A.K., Messali, M., Ali, I., Aouad, M.R., 2020. Synthesis, characterization, DNA binding, anticancer, and molecular docking studies of novel imidazolium-based ionic liquids with fluorinated phenylacetamide tethers. ACS Omega 5, 4807–4815.

Saha, S., Sultana, S., Islam, M.M., Rahman, M.M., Mollah, M.Y.A., Susan, M.A.B.H., 2014. Electrodeposition of cobalt with tunable morphology from reverse micellar solution. Ionics (Kiel) 20 (8), 1175–1181.

Shivakumara, S., Naik, Y.A., Achary, G., Sachin, H.P., Venkatesha, T.V., 2008. Influence of condensation product on electrodeposition of Zn-Mn alloy on steel. IJCT. 15, 29–35.

Sorour, N., Zhang, W., Ghali, E., Houlachi, G., 2017. A review of organic additives in zinc electrodeposition process (performance and evaluation). Hydrometallurgy 171, 320–332.

Sulaiman, K.O., Onawole, A.T., Faye, O., Shuaib, D.T., 2019. Understanding the corrosion inhibition of mild steel by selected green compounds using chemical quantum based assessments and molecular dynamics simulations. J. Mol. Liq. 279, 342–350.

Sun, Y., Wang, Z., Wang, Y., Liu, M., Li, S., Tang, L., Wang, S., Yang, X., Ji, S., 2020. Improved transport of gold (I) from aurocyanide solution using a green ionic liquid-based polymer inclusion membrane with in-situ electrodeposition. Chem. Eng. Res. Des. 153, 136–145.

Vijayakumar, J., Mohan, S., Kumar, S.A., Suseendiran, S.R., Pavithra, S., 2013. Electrodeposition of Ni–Co–Sn alloy from choline chloride-based deep eutectic solvent and characterization as cathode for hydrogen evolution in alkaline solution. Int. J. Hydrogen Energy 38 (25), 10208–10214.

Wang, J., Wang, Y., Xie, T., Deng, Q., 2019. Facile and fast synthesis of Ni composite coating on Ti mesh by electrodeposition method for high-performance hydrogen production. Mater. Lett. 245, 183–1141.

Zhang, Q., Hua, Y., 2012. Kinetic investigation of zinc electrodeposition from sulfate electrolytes in the presence of impurities and ionic liquid additive [BMIM] HSO4. Mater. Chem. Phys. 134 (1), 333–339.

Zohdy, K.M., El-Shamy, A.M., Kalmouch, A., Gad, E.A.M., 2019. The corrosion inhibition of (2Z, 2′ Z)-4, 4′-(1, 2-phenylene bis (azanediyl)) bis (4-oxobut-2-enoic acid) for carbon steel in acidic media using DFT. Egypt. J. Pet. 28 (4), 355–359.